Full-Envelope Stitched Simulation Model of a Quadcopter Using STITCH

Eric L. Tobias
Senior Research Engineer
Frank C. Sanders
Research Associate
San Jose State University
U.S. Army Aviation Development Directorate
(AMRDEC)
Moffett Field, CA, USA

Mark B. Tischler
Senior Scientist
U.S. Army Aviation Development Directorate
(AMRDEC)
Moffett Field, CA, USA

ABSTRACT

Accurate real-time simulation models of small-scale multi-rotor vehicles are desirable for full-mission simulation and flight control evaluations within hardware-in-the-loop simulation. This paper presents the development and verification of a continuous, full-envelope stitched simulation model of a quadcopter using flight-identified models of the 3D Robotics IRIS+ and the newly-developed model stitching simulation software STITCH. Two flight-identified point models (one at hover and one at forward flight), plus some additional trim data, are shown herein to adequately and accurately capture the bare-airframe dynamics of the IRIS+ over its nominal flight envelope. The stitched simulation model is verified in the frequency domain for multiple airspeeds. Additionally, the off-nominal mass-, CG-, and inertia-extrapolation capabilities of STITCH are investigated and the results are verified against flight data for a heavy loading configuration. The overall findings are considered to provide flight-test guidance for the development of stitched simulation models of small-scale multi-rotor vehicles.

INTRODUCTION

Linear state-space perturbation models, which represent the dynamic response of an aircraft for a discrete reference flight condition and configuration, are accurate within some limited range of the reference condition. These discrete-point linear models, as derived from system identification from flight testing, for example, are suitable for point control-system design and point handling qualities analyses; however, continuous, full-envelope simulation is desirable for full-mission and hardware-in-the-loop simulation.

Model stitching is the technique of combining or "stitching" together individual linear models and trim data for discrete flight conditions to produce a continuous, full flight-envelope simulation model (Ref. 1). In this technique, the dimensional stability and control derivatives and trim data for each discrete point model are stored as a function of key parameters such as airspeed and altitude. The look-up of trim and derivatives is combined with nonlinear equations of motion and nonlinear gravitational force equations to produce a continuous, quasi-nonlinear, *stitched* simulation model. The theoretical concept of the model stitching technique has been applied to develop a *model stitching simulation architecture* (Ref. 2), which incorporates extrapolation methods for the simulation of off-nominal aircraft loading configurations, including variations in weight, inertia, and center of gravity.

Presented at the AHS International 74th Annual Forum & Technology Display, Phoenix, Arizona, USA, May 14–17, 2018.
This is a work of the U.S. Government and is not subject to copyright protection in the U.S.
Distribution A. Approved for public release. Distribution is unlimited.

Zivan and Tischler (Ref. 3) built on the early work of model stitching and produced a stitched model of the Bell 206 helicopter from a series of flight-identified point models. Several notable stitched models have been developed over the last decade (Ref. 2). Greiser and Seher-Weiss (Ref. 4) developed a stitched model of DLR's ACT/FHS, which is a highly-modified EC135, from five flight-identified high-order linear models. Most recently, Berger et al. (Ref. 5) developed a full flight-envelope stitched model of the Calspan Variable Stability Learjet-25, and Knapp et al. (Ref. 6) developed a full flight-envelope stitched model of the Calspan F-16 VISTA, both from flight data.

A new software capability called STITCH is being developed by the U.S. Army Aviation Development Directorate, which allows a non-expert to create and verify a stitched model from point models and trim data. STITCH incorporates a graphical user interface (GUI) and anticipatory design elements to guide the user through the process of generating a stitched model, from setup of the project and loading of the data to verification and utilization of the stitched model. The model stitching simulation environment STITCH is applicable to any flight vehicle for which point-wise linear models and trim data can be obtained, and is demonstrated herein with flight-identified models of the IRIS+ quadcopter.

This paper first covers the basic concepts of model stitching and an overview of the model stitching simulation architecture. A preview of the forthcoming software capability STITCH is presented. Then, the details of the frequency-domain-based system identification process and results for flight-identified models of the IRIS+ are presented. The development and verification of a stitched simulation model of

a quadcopter using STITCH with the flight-identified point models of the IRIS+ is then covered. Additionally, the extrapolation capabilities for off-nominal loading are verified against flight data for a heavy loading configuration. Finally, this paper presents flight-test recommendations for future development of stitched models involving small-scale multirotor vehicles.

MODEL STITCHING SIMULATION ARCHITECTURE

A comprehensive model stitching simulation architecture has been developed (Ref. 2), which allows continuous, full flight-envelope simulation based on a collection of discrete-point linear models and trim data. Individual linear models and associated trim data for specific flight conditions are tabulated and incorporated with nonlinear elements to produce a continuous, quasi-nonlinear simulation model. Extrapolation methods within the model stitching architecture permit accurate simulation of off-nominal aircraft loading configurations, including variations in weight, inertia, and center of gravity, and variations in altitude, which together minimize the required number of point models for full-envelope simulation. Additional modeling elements are incorporated, including turbulence and a standard atmosphere model, as well as accommodations for user-specified modeling components such as engine models and landing gear.

Model Stitching Basic Concepts

The key requirement for model stitching is a series of state-space models and associated trim data of the states and controls for point flight conditions, or "anchor" point models, covering a range of airspeed. The point models and trim data may be identified from flight testing or derived from a more complex, non-realtime model, for example.

Following Ref. 1, given a linear model of a specific aircraft configuration, the generalized state-space representation is utilized to give the appropriate perturbation dynamic response about a *reference flight condition* (i.e., anchor point) with trim x-body airspeed U_0:

$$\dot{\boldsymbol{x}} = \boldsymbol{A}|_{U_0}\boldsymbol{x} + \boldsymbol{B}|_{U_0}\boldsymbol{u} \tag{1}$$

$$\boldsymbol{y} = \boldsymbol{C}|_{U_0}\boldsymbol{x} + \boldsymbol{D}|_{U_0}\boldsymbol{u} \tag{2}$$

which is expressed in terms of the dimensional stability and control derivatives for the reference flight condition (i.e., the $\boldsymbol{A}$, $\boldsymbol{B}$, $\boldsymbol{C}$, and $\boldsymbol{D}$ matrices from the state-space model in body axes for trim x-body airspeed U_0), the perturbation state vector $\boldsymbol{x}$, and the perturbation control vector $\boldsymbol{u}$.

The state-space representation is then rewritten in terms of the vector of total values of states $\boldsymbol{X}$, vector of total values of controls $\boldsymbol{U}$, and vector of total values of outputs $\boldsymbol{Y}$ rather than perturbation values, and at the *instantaneous* x-body airspeed U instead of reference trim x-body airspeed U_0. Vectors of trim states $\boldsymbol{X}_0$ and trim controls $\boldsymbol{U}_0$ are included forming a continuous, full flight-envelope simulation model by expressing the state-space equations as

$$\dot{\boldsymbol{X}} = \boldsymbol{A}|_U\left(\boldsymbol{X} - \boldsymbol{X}_0|_U\right) + \boldsymbol{B}|_U\left(\boldsymbol{U} - \boldsymbol{U}_0|_U\right) \tag{3}$$

$$\boldsymbol{Y} = \boldsymbol{C}|_U\left(\boldsymbol{X} - \boldsymbol{X}_0|_U\right) + \boldsymbol{D}|_U\left(\boldsymbol{U} - \boldsymbol{U}_0|_U\right) + \boldsymbol{Y}_0|_U \tag{4}$$

For "stitching in U," all trim data and stability and control derivative values are tabulated and subsequently interpolated as a function of instantaneous x-body airspeed U. That is,

$$\left(W_0|_U,\ \Phi_0|_U,\ \Theta_0|_U,\ \delta_{\text{lat}_0}|_U,\ \delta_{\text{lon}_0}|_U,\ \ldots\right) = f(U) \tag{5}$$

$$\left(\boldsymbol{A}|_U,\ \boldsymbol{B}|_U,\ \boldsymbol{C}|_U,\ \boldsymbol{D}|_U\right) = f(U) \tag{6}$$

where trim z-body airspeed W_0, trim roll attitude Φ_0, trim pitch attitude Θ_0, trim lateral stick δ_{lat_0}, and trim longitudinal stick δ_{lon_0} are used in this example.

As expected from Equations (3) and (4), at reference speed of $U = U_0$, the continuous simulation will trim ($\dot{\boldsymbol{X}} = 0$) with model states, controls, and outputs at the anchor point values:

$$\boldsymbol{X} = \boldsymbol{X}_0|_U \tag{7}$$

$$\boldsymbol{U} = \boldsymbol{U}_0|_U \tag{8}$$

$$\boldsymbol{Y} = \boldsymbol{Y}_0|_U \tag{9}$$

which is crucial for good fidelity in piloted or hardware-in-the-loop simulation.

As u is included as a state, a subtle yet important detail becomes evident from Eq. (3). All stability derivatives for forward speed perturbation u (i.e., X_u, Z_u, M_u, etc.) are nulled-out (multiplied by 0) because the instantaneous x-body airspeed U (the query for the lookup table) and the returned table value of x-body airspeed are always identical (i.e., $U_0|_U = U$ and therefore $U - U_0|_U = 0$). However, the effect of these nulled-out derivatives is preserved and is contained *implicitly* in the speed variation of the trim states and controls, so the dynamic response of the anchor point model is maintained.

The effective, *implicit representation* of the speed derivatives X_u, Z_u, and M_u are given as (Ref. 2)

$$\begin{aligned} X_u = {} & g\cos\Theta_0|_U\left(\frac{\partial\Theta_0|_U}{\partial u}\right) - X_w|_U\left(\frac{\partial W_0|_U}{\partial u}\right) \\ & - X_{\delta_{\text{lon}}}|_U\left(\frac{\partial\delta_{\text{lon}_0}|_U}{\partial u}\right) - X_{\delta_{\text{col}}}|_U\left(\frac{\partial\delta_{\text{col}_0}|_U}{\partial u}\right) \end{aligned} \tag{10}$$

$$\begin{aligned} Z_u = {} & g\sin\Theta_0|_U\left(\frac{\partial\Theta_0|_U}{\partial u}\right) - Z_w|_U\left(\frac{\partial W_0|_U}{\partial u}\right) \\ & - Z_{\delta_{\text{lon}}}|_U\left(\frac{\partial\delta_{\text{lon}_0}|_U}{\partial u}\right) - Z_{\delta_{\text{col}}}|_U\left(\frac{\partial\delta_{\text{col}_0}|_U}{\partial u}\right) \end{aligned} \tag{11}$$

$$\begin{aligned} M_u = {} & -M_w|_U\left(\frac{\partial W_0|_U}{\partial u}\right) - M_{\delta_{\text{lon}}}|_U\left(\frac{\partial\delta_{\text{lon}_0}|_U}{\partial u}\right) \\ & - M_{\delta_{\text{col}}}|_U\left(\frac{\partial\delta_{\text{col}_0}|_U}{\partial u}\right) \end{aligned} \tag{12}$$

This concept of implicit speed derivatives is fundamental to the model stitching technique, and will be referenced and verified in the quadcopter stitched model results herein.

Key Simulation Elements

In the model stitching simulation architecture, the basic concepts of the model stitching technique are formulated as a block diagram and combined with nonlinear equations of motion and other simulation elements. Figure 1 shows a top-level schematic of the model stitching simulation architecture. The key elements are briefly discussed below. See Ref. 2 for a detailed discussion of the model stitching simulation elements.

State and Control Perturbations Given the current x-body airspeed U, look-ups are performed to find the vectors of trim aircraft states $\boldsymbol{X}_0$ and trim controls $\boldsymbol{U}_0$. With the current aircraft state vector $\boldsymbol{X}$ and current control vector $\boldsymbol{U}$, the state perturbation vector $\Delta\boldsymbol{x}$ and control perturbation vector $\Delta\boldsymbol{u}$ are found:

$$\Delta\boldsymbol{x} \equiv \boldsymbol{X} - \boldsymbol{X}_0|_U \tag{13}$$

$$\Delta\boldsymbol{u} \equiv \boldsymbol{U} - \boldsymbol{U}_0|_U \tag{14}$$

This arithmetic is shown schematically in Figure 1 at labels ① and ②.

Aerodynamic Perturbation Forces and Moments Aerodynamic perturbation forces and moments are calculated based on the state and control perturbation vectors found in Equations (13) and (14) and the dimensional stability and control derivatives at the current airspeed. For use in the model stitching architecture, we introduce the aerodynamic matrices $\boldsymbol{A}_{\text{aero}}$ and $\boldsymbol{B}_{\text{aero}}$ that contain the dimensional stability and control derivatives only; they do not contain gravity or Coriolis terms. These matrices also do not include Euler angle states $\begin{bmatrix}\phi & \theta & \psi\end{bmatrix}$ as kinematics are included in the nonlinear equations of motion.

Next, the dimensional mass matrix $\boldsymbol{M}$, which is comprised of the flight-test values for aircraft mass m and inertia tensor $\boldsymbol{I}$, is multiplied into the matrix of stability derivatives $\boldsymbol{A}_{\text{aero}}$ and the state perturbation vector $\Delta\boldsymbol{x}$ to yield a vector of aerodynamic dimensional perturbation forces and moments. Likewise, the mass matrix is multiplied into the matrix of control derivatives $\boldsymbol{B}_{\text{aero}}$ and the control perturbation vector $\Delta\boldsymbol{u}$ to produce a vector of dimensional perturbation control forces and moments. The sum of both vectors yields the complete aerodynamic dimensional perturbation forces and moments, as shown schematically in Figure 1 by labels numbered ③.

Aerodynamic Trim Forces This simulation element determines the dimensional aerodynamic trim forces based on the trim aircraft attitude at the current airspeed. A lookup is first performed to find the trim Euler angles at the current x-body airspeed U (i.e., the trim pitch attitude at the current airspeed, $\Theta_0|_U$, and the trim roll attitude at the current airspeed, $\Phi_0|_U$). The *specific* aerodynamic trim forces are obtained as (Ref. 7)

$$\bar{X}_{\text{aero}_0} = g\sin\Theta_0|_U \tag{15}$$

$$\bar{Y}_{\text{aero}_0} = -g\cos\Theta_0|_U \sin\Phi_0|_U \tag{16}$$

$$\bar{Z}_{\text{aero}_0} = -g\cos\Theta_0|_U \cos\Phi_0|_U \tag{17}$$

where g is acceleration due to gravity. The specific aerodynamic trim forces are then multiplied by the aircraft mass m to obtain the dimensional aerodynamic trim forces, shown schematically in Figure 1 at label ④.

Total Aerodynamic Forces and Moments The aerodynamic dimensional perturbation forces and moments [labels numbered ③] are summed with the dimensional aerodynamic trim forces [label ④] to yield the total aerodynamic forces and moments. This summation is shown graphically at label ⑤ in Figure 1.

Nonlinear Gravitational Forces The model stitching simulation architecture incorporates nonlinear kinematics (small angle approximations are not made). Therefore, the *specific* gravity forces acting at the aircraft CG are nonlinear with respect to the aircraft Euler angles, and are computed as follows (Ref. 7):

$$\bar{X}_{\text{grav}} = -g\sin\Theta \tag{18}$$

$$\bar{Y}_{\text{grav}} = g\cos\Theta\sin\Phi \tag{19}$$

$$\bar{Z}_{\text{grav}} = g\cos\Theta\cos\Phi \tag{20}$$

It is important to emphasize that no look-up of trim data is performed for the gravitational force computation, but rather the current, instantaneous values of the aircraft pitch attitude Θ and roll attitude Φ are used in the computation. At trim, note that the specific aerodynamic trim forces [Eqs. (15)–(17)] must balance these specific gravity forces. The specific gravity forces are then multiplied by the current *simulation value* of aircraft mass m_{sim} to obtain the dimensional gravity forces. The dimensional gravity force calculation is shown at label ⑥ in Figure 1. The current simulation value of aircraft mass m_{sim}, which is not necessarily the same mass value associated with the baseline/identified anchor point models, is utilized here to simulate off-nominal aircraft weight. A discussion of off-nominal weight extrapolation as applied to the IRIS+ stitched model is presented later in this paper.

Total Forces and Moments The aerodynamic forces and moments [label ⑤] are summed with the gravity forces [label ⑥] to yield the total external, dimensional forces and moments acting at the CG. This summation is shown schematically at label ⑦ in Figure 1. The total forces and moments may be augmented with user-specified external forces and moments for the simulation of additional modeling components (e.g., landing gear).

Nonlinear Equations of Motion Incorporated in the model stitching simulation architecture is the nonlinear representation of Newton's equations of motion in the body-fixed (Eulerian) frame. Given the total forces and moments about the aircraft CG [label ⑦] and the simulation values of mass and inertia (m_{sim} and $\boldsymbol{I}_{\text{sim}}$), the 6-DOF body-axes nonlinear equations of motion are implemented to obtain the state-dot vector $\dot{\boldsymbol{X}}$,

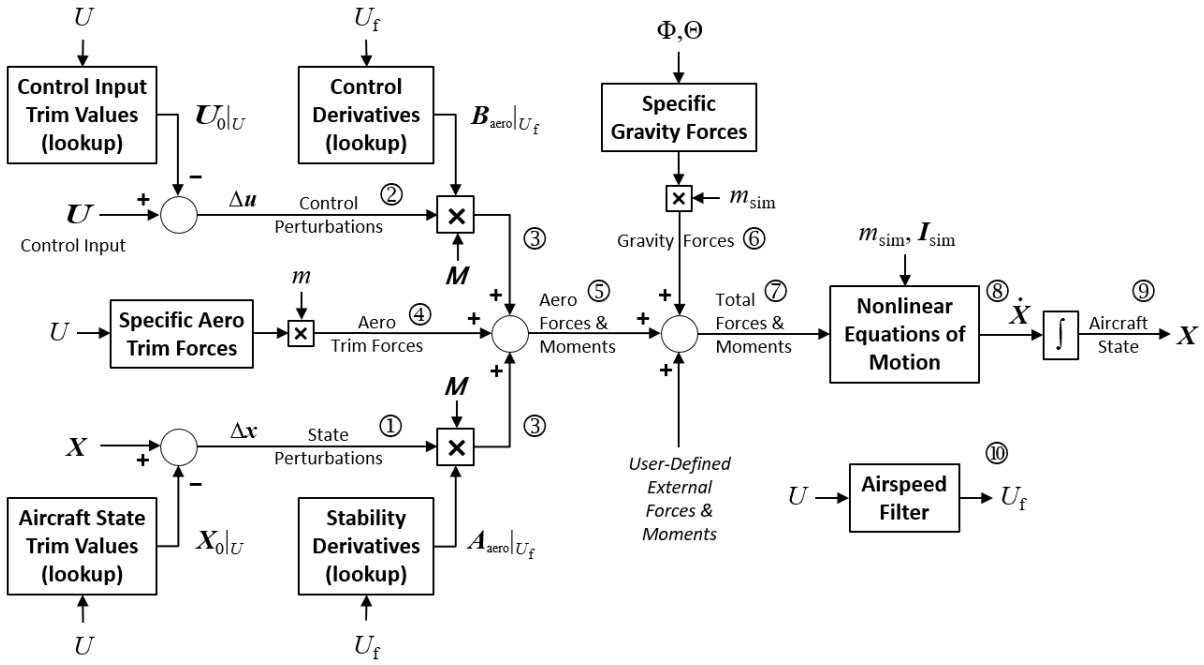

Fig. 1. Model stitching simulation architecture – top level schematic.

shown at label ⑧ in Figure 1). The equations of motion contain the nonlinear Euler equations, which include the cross-coupling inertial and Coriolis terms in full nonlinear form. The state-dot vector is then integrated to obtain the updated aircraft state vector $\boldsymbol{X}$, as depicted at label ⑨.

Airspeed Filter A first-order low-pass filtered airspeed is used for look-up of the stability and control derivatives only; *not* the trim data. Applying the filter ensures that the derivative values remain constant for short-term motion, thereby retaining accurate dynamic responses at the anchor points. The airspeed filter and output filtered x-body airspeed U_f are shown schematically at label ⑩ in Figure 1. A break frequency of $\omega_\mathrm{f} = 0.2$ rad/sec has been found to be satisfactory, in that it corresponds to the lower end of the frequency range of applicability for most identified models and yet is still fast enough to allow accurate simulation of moderately-aggressive acceleration/deceleration (Ref. 1). A higher break frequency may be appropriate for applications involving small aircraft, in which the flight envelope can be flown through rapidly.

Extrapolation for Loading Configuration

A powerful feature of the model stitching architecture is the ability to accurately simulate off-nominal aircraft loading configurations without the need for additional data (Ref. 2). For the current effort, the effects on trim and dynamic response of the IRIS+ configured with a payload are investigated. These predicted weight-, CG-, and inertia-extrapolation results of the model stitching simulation architecture are verified against truth flight-test data.

STITCH SOFTWARE

A new software capability called STITCH is being developed by the U.S. Army Aviation Development Directorate. STITCH allows a non-expert to create and verify a stitched simulation model from point models and trim data, and is applicable for any flight vehicle for which point-wise linear models and trim data can be obtained. STITCH is currently in Beta development, with an anticipated Beta release in July 2018.

In addition to providing a user interface front end to the model stitching simulation architecture, STITCH features anticipatory design elements to guide the user through the process of generating a stitched model—from setup of the project and loading of the data to verification and utilization of the stitched model. A summary of STITCH features include:

- Graphical user interface (GUI)
- Processing of raw flight-test data
- Automated generation/verification of the stitched model
- Interactive plotting utilities
- Batch processing for families of cases

Figures 2–4 present a few example screenshots of STITCH.

For the current effort, STITCH was used to develop a stitched simulation model of the IRIS+ quadcopter. The key steps, which include processing the flight-identified anchor point data, verifying the stitched model, and utilizing the extrapolation features for off-nominal loading configuration, are presented later in this paper.

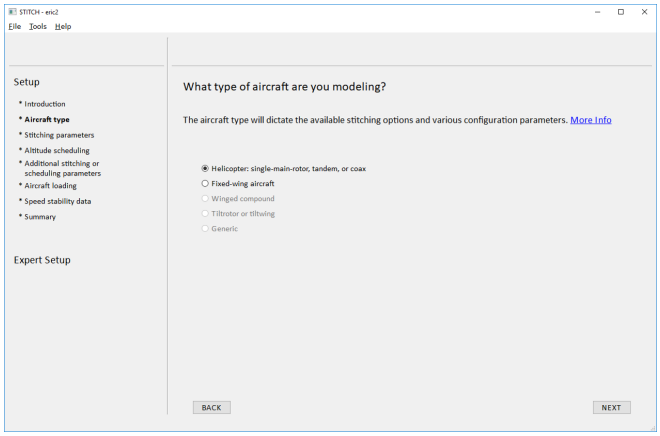

Fig. 2. STITCH example screenshot: selection of aircraft type in project setup.

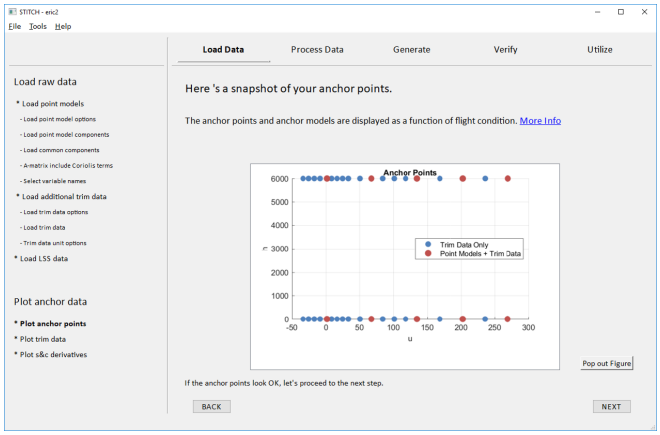

Fig. 3. STITCH example screenshot: overview of anchor points.

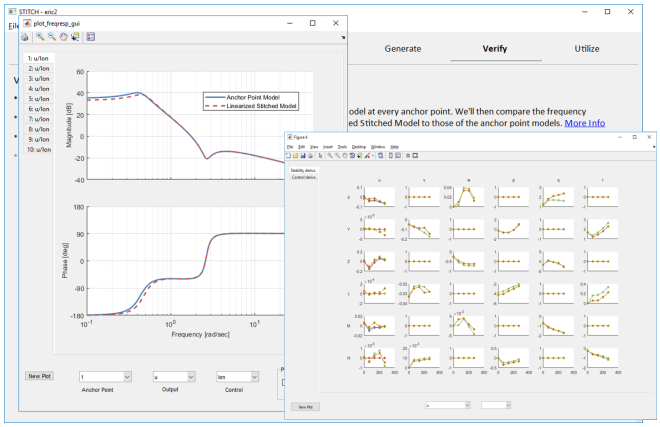

Fig. 4. STITCH example screenshot: plot tools for verification frequency responses and derivatives.

FLIGHT-IDENTIFIED MODELS OF THE IRIS+ QUADCOPTER

Accurate bare-airframe models of the vehicle, which consist of the IRIS+ airframe, mixer, and motors, in hover (Ref. 8) and forward-flight were identified from flight data using the U.S. Army Aviation Development Directorate developed software package CIFER® (Ref. 1). Frequency sweep inputs and aircraft states were recorded to generate frequency responses spanning 0.5–60 rad/sec. From these frequency responses, state-space models of the aircraft in hover and 17 kts forward flight were generated for use in the stitched model.

Aircraft Description

The 3D Robotics IRIS+, as shown in Figure 5, is a quadrotor configuration that measures 19.75 inches diagonally motor-to-motor, has a total flying weight of approximately 3.2 lb, a payload capacity of 0.9 lb, and an average flight time of approximately 16 min (Ref. 9). The aircraft features the open-source Pixhawk 1 flight computer running ArduPilot-based ArduCopter firmware. In order to verify the extrapolation capabilities of the stitched model, the aircraft was flown in two loading configurations: nominal and heavy. The heavy configuration featured a 0.441-lb cylinder ($\approx 50\%$ of load capacity) strapped to the underside of the aircraft, as shown in Figure 6.

Fig. 5. The 3D Robotics IRIS+.

Flight Data Collection

System identification flights in hover and forward flight were conducted with the use of automated frequency sweep inputs. The automated frequency sweeps were injected just upstream of the mixer, as illustrated in Figure 7, to excite the bare-airframe directly. The automated sweep allowed the pilot to engage and disengage the sweep by simply flipping a switch. With the control system engaged, logging of the total mixer inputs enables identification of the bare-airframe dynamics (e.g., p/δ_{lat}).

The GPS velocity measurements were used to provide trim airspeed data (not used for dynamic response) as the aircraft

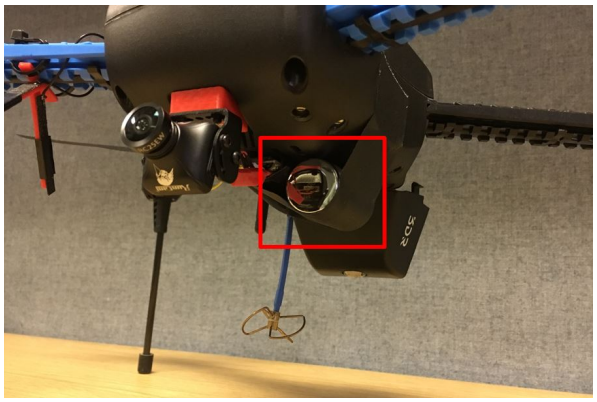

Fig. 6. Detail of the 200-gram cylinder strapped to the aircraft in the heavy loading configuration.

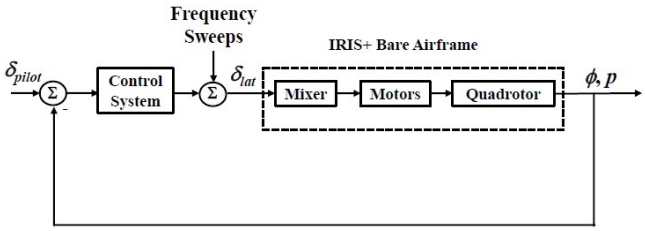

Fig. 7. Schematic showing injection of frequency sweeps for bare-airframe identification (Ref. 8).

was flown in zero wind conditions throughout the data collection flights and no airspeed measurements were available. Each axis was swept individually, and in hover the process was relatively straightforward as the pilot simply held position over the ground. To ensure a consistent forward-flight velocity, the aircraft pitch attitude was commanded through a switch on the radio transmitter. From hover, the pilot engaged the forward-flight longitudinal trim setting switch, waited until the aircraft reached steady state, and then engaged the automated sweep. Once in forward-flight, the aircraft was kept in forward-flight for the remaining data collection points in each axis. To keep the aircraft within line-of-site while in forward-flight, a racetrack pattern was flown. The flight test process was then repeated in the heavy loading configuration for verification data. This flight test methodology was found to provide consistent velocities and attitudes and resulted in excellent flight data, as seen in the high coherence of Figure 8.

Steady-state trim data for use in the stitched model were collected from hover to 32 kts. The commanded attitude was varied in 5 degrees nose down increments via the transmitter's longitudinal trim. In total, six anchor trim points at a spacing of about 6 kts were collected in both nominal and heavy loading configurations.

Identified Model in Hover

The hover bare-airframe identification model used in this analysis was obtained in a prior U.S. Army Aviation Development Directorate project and can be found in Refs. 8 and 10. The identified hover derivatives are shown later in Table 3.

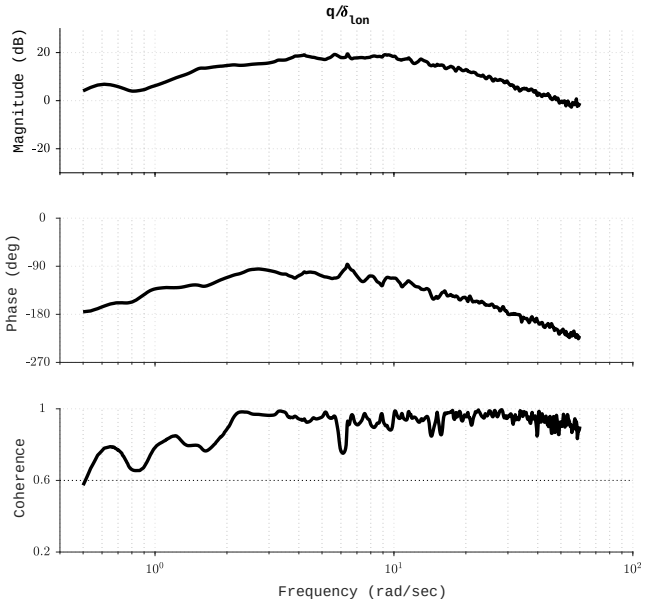

Fig. 8. Typical forward-flight frequency response showing excellent coherence over entire frequency range.

Identified Model in Forward-Flight

The frequency responses obtained from flight were used to generate a state-space model with the CIFER® DERIVID tool. Model structure determination was completed based on data coherence, parameter insensitivities and Cramér-Rao bounds (Ref. 1).

The identified aerodynamic stability derivatives (Coriolis terms not included), control derivatives, and time delays for the 17-kt forward-flight model are shown in Table 1. Figure 9 shows excellent agreement of the identified model overlaid with the flight data in the frequency domain, and Table 2 supports the fidelity of the model with excellent individual and average costs. The average model cost was 48.9 (rotorcraft model costs < 100 considered excellent (Ref. 1)). The time-domain verification of the identified model, using dissimilar data not used in the identification, is presented in Figure 10 and shows the excellent agreement of the model and flight data once again. The acceptable cost of the time-domain verification, according to the guidelines of Ref. 1, is $J_{rms} \leq 1$ to 2, and the cost of the IRIS+ 17-kt forward-flight model time-domain verification was $J_{rms} = 5.46$. This discrepancy is due to the small scale of the aircraft, and if the guidelines' range is scaled down by multiplying the full scale range by the square root of the Froude scale factor N=32.6 (Froude scaling and the Froude Scale factor are discussed in depth in a later section), then the acceptable range becomes $J_{rms_{Fr}} \leq 5$ to 11. Thus the identified IRIS+ 17-kt model's time-domain verification cost is acceptable by the Froude-scaled acceptability range.

Nearly all of the identified derivatives' Cramér-Rao bounds and insensitivities fall within the frequency-domain system identification guidelines (Ref. 1), and a few derivatives are acceptably close. The Cramér-Rao bounds and insensitivity

of M_q lie outside of the recommended limits; however, the derivative was included in the model because the omission of the term led to an unacceptably large jump in the individual costs of longitudinal responses and a poor model fit in the time domain. Additionally, the symmetry of the aircraft can be seen in the similarity of the values of X_u and Y_v. The symmetry of the aircraft is also apparent in the values of the damping derivatives L_p and M_q, despite the high bounds. A more accurate value of M_q may be achieved by enforcing symmetry in the identification process, but for the purposes of this research the original identified value was retained.

Table 1. Identified Parameters of the 17-kt IRIS+ Model (No Coriolis Terms)

Derivative	Value	C.R. (%)	Insens. (%)
X_u [a]	−0.2956	-	-
Y_v [a]	−0.2346	-	-
Z_w	−0.8271	5.6	2.1
Z_q	−1.1668	20.9	9.3
L_p	−1.2161	24.8	11.4
M_u	0.3172	21.6	9.2
M_w	1.6648	7.6	1.7
M_q	−1.0854	51.4	19.4
N_r	−1.7768	18.8	6.1
$X_{\delta_{\text{lon}}}$	−9.9573	4.5	1.8
$Y_{\delta_{\text{lat}}}$	6.2517	5.1	2.0
$L_{\delta_{\text{lat}}}$	85.5219	3.5	1.4
$M_{\delta_{\text{lon}}}$	121.0780	4.4	0.9
$N_{\delta_{\text{ped}}}$	5.6798	4.9	1.7
$Z_{\delta_{\text{col}}}$	−35.2408	3.9	1.4
τ_{lat}	0.01755	6.2	2.5
τ_{lon}	0.01829	5.8	2.3
τ_{col}	0.01585	8.0	3.4

[a] Fixed value in ID model from TF fits (e.g., $\dot{u}/q$)

Table 2. Identified Model Costs for the 17-kt Identification of the IRIS+

Response	Cost
$\dot{v}/\delta_{\text{lat}}$	39.4
p/δ_{lat}	27.8
a_y/δ_{lat}	40.6
$\dot{u}/\delta_{\text{lon}}$	41.8
$\dot{w}/\delta_{\text{lon}}$	29.7
q/δ_{lon}	50.9
a_x/δ_{lon}	45.4
a_z/δ_{lon}	85.9
$\dot{v}/\delta_{\text{ped}}$	47.3
r/δ_{ped}	57.6
$\dot{w}/\delta_{\text{col}}$	64.9
a_z/δ_{col}	54.9
J_{ave}	48.9

Comparison of Hover and Forward-Flight Model

Table 3 shows the comparison of the identified aerodynamic stability derivatives and control derivatives of the IRIS+ in hover and forward flight. It can be seen that the dynamics in hover are driven solely by the translational velocity terms, while in forward flight the angular rate damping terms become active. Table 4 shows the comparison of the hover and forward-flight eigenvalues and their respective modes/axes. In hover, the unstable phugoid and real pole in both pitch and roll axes were present for the IRIS+. In the roll axis during forward flight, the lateral hovering cubic breaks into two stable, real poles. In the pitch axis during forward flight, the longitudinal hovering cubic broke into four real poles. Two of the poles occur at low frequency, suggesting a phugoid mode, and two occur near the break frequency of the on-axis q/δ_{lon} response, suggesting a short period mode. One of the low frequency poles and one of the high frequency poles of the four longitudinal poles are unstable.

A time vector diagram (Ref. 1) was generated to compare the longitudinal short period modes of hover and forward flight and is shown in Figure 11. This time vector diagram provides insight into the relative contribution of each term in the equations of motion for a specific eigenvalue. For example, the $\dot{q}$ response is written as

$$\dot{q} = M_u u + M_q q + M_w w \tag{21}$$

The time vector equation is then formulated by taking the Laplace transform of Eq. 21, substituting the eigenvalue, the unnormalized eigenvector associated with the mode, and the identified, dimensional stability derivatives, then the equation is normalized by the largest component (Ref. 1). Figure 11 shows the relative contributions of the aerodynamic terms balanced by the inertial forces $\dot{u}, \dot{w}$, or $\dot{q}$. The upper portion of Figure 11 shows the $\dot{u}, \dot{w}$, and $\dot{q}$ equations of motion and associated terms for the eigenvalue in hover, while the lower portion represents the same equations of motion and associated terms for the comparable eigenvalue in forward flight. It can be seen in the time vector diagram that in hover the translational velocity term of the $\dot{u}$ has a relatively small contribution compared to the gravity term, the angular rate damping terms are not present in the $\dot{u}$ and $\dot{q}$ equations, and there is no $\dot{w}$ equation. In forward flight, the equations have angular rate damping terms present and the gravity terms of $\dot{u}$ and $\dot{w}$ are significantly reduced in magnitude compared to hover. The forward-flight $\dot{w}$ equation shows a large contribution from the $(U_0 + Z_q)q$ term, however, the Coriolis term U_0 is significantly larger than the rate damping term and shows that aerodynamics have comparatively little effect in the $\dot{w}$ response.

FROUDE SCALING INSIGHTS

Froude scaling provides a method to gain insight into small scale aircraft dynamics by scaling down full scale aircraft dynamics. The XV-15 tiltrotor aircraft best approximates the configuration of the IRIS+ in the lateral axis, due to the low

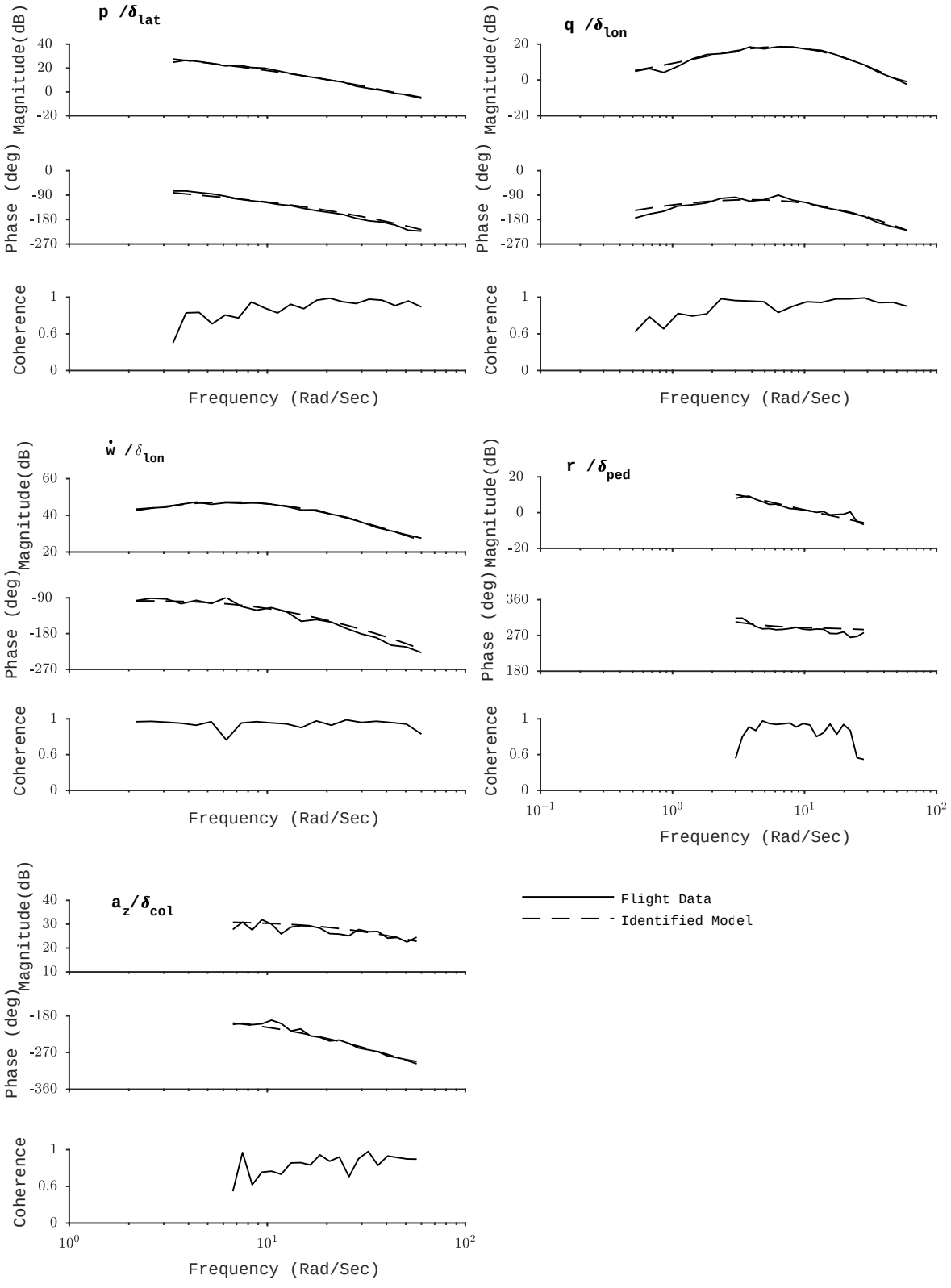

Fig. 9. Frequency response comparison of identified model overlaid with 17-kt forward-flight flight data.

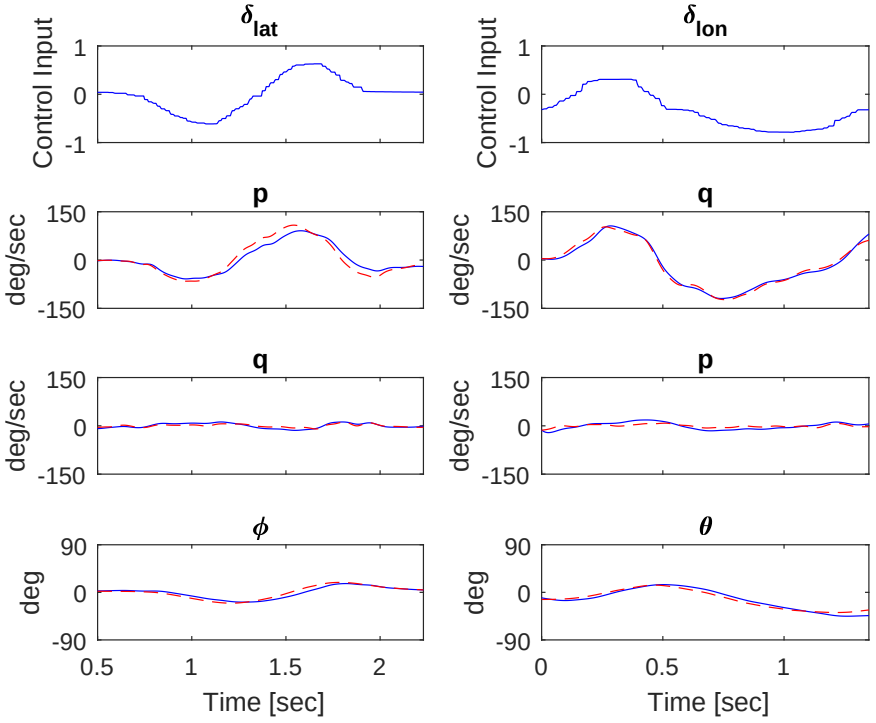

Fig. 10. Time-domain verification of the identified IRIS+ 17-kt model ($J_{RMS} = 5.49$). Dashed line is identified model and solid line is flight data.

Table 3. Comparison of Stability and Control Derivatives of the Hover and 17-kt Models of the IRIS+

Derivative	Hover	17 kts	Difference
X_u	−0.3246	−0.2956	9.4%
Y_v	−0.1996	−0.2346	16.1%
Z_w	0	−0.8271	-
Z_q	0	−1.1668	-
L_v	−0.5363	0	-
L_p	0	−1.2161	-
M_u	1.7355	0.3172	138.2%
M_w	0	1.6648	-
M_q	0	−1.0854	-
N_r	0	−1.7768	-
$X_{\delta_{\text{lon}}}$	−7.5513	−9.9573	27.5%
$Y_{\delta_{\text{lat}}}$	6.4016	6.2517	2.4%
$L_{\delta_{\text{lat}}}$	80.0269	85.5219	6.6%
$M_{\delta_{\text{lon}}}$	92.1241	121.0780	27.2%
$N_{\delta_{\text{ped}}}$	5.6427	5.6798	0.7%
$Z_{\delta_{\text{col}}}$	−60.7660	−35.2408	53.2%

mast height and differential collective for roll control. The additive rotor dynamics are minimal, so the differential collective closely resembles the mechanism in which the IRIS+ is controlled in roll. When compared rotor-to-rotor, 57 ft for the XV-15 rotorcraft versus 19.75 inches for the IRIS+ gives a Froude scale factor N=34.7. The Froude scaled frequencies and velocities are then obtained by (Ref. 11):

$$\omega_{\text{Froude Scale}} = \omega_{\text{Full Scale}}\sqrt{N} \tag{22}$$

Table 4. Eigenvalues and Modes in Hover and 17 kts

Hover	Mode	17 kts	Mode
[−0.48, 2.55]	Roll	(0.235)	Spiral
(2.65)	Roll	(1.22)	Roll Aperiodic
		(0)	Roll
(0)	Yaw	(1.78)	Yaw
[−0.48, 3.77]	Phugoid	(−0.163)	Phugoid
(3.93)	Short Period	(0.554)	Phugoid
(0)	Heave	(−6.02)	Short Period
		(7.84)	Short Period

$[\zeta, \omega] = s^2 + 2\zeta\omega s + \omega^2$, $(a) = (s + a)$

$$V_{\text{Froude Scale}} = V_{\text{Full Scale}}/\sqrt{N} \tag{23}$$

Table 5 provides a comparison of the XV-15 lateral hover modes and their frequencies (Ref. 1), the Froude-scaled values, and the identified hover modes and frequencies of the IRIS+. The Froude-scaled values of the XV-15 lateral axis modal frequencies are within 7.5% and 35.6% of the identified IRIS+ hover frequencies. This suggests that Froude scaling modal frequencies in hover, based on rotor-to-rotor distance ratios, provides a good basis in which to predict and understand small scale aircraft dynamics. While this Froude scale comparison was solely done in hover and a single axis, a similar forward-flight analysis could be performed provided forward-flight data existed for a full scale representative aircraft.

Froude scaling of the full scale UH-60 point model separation velocities gives insight into the number of point models nec-

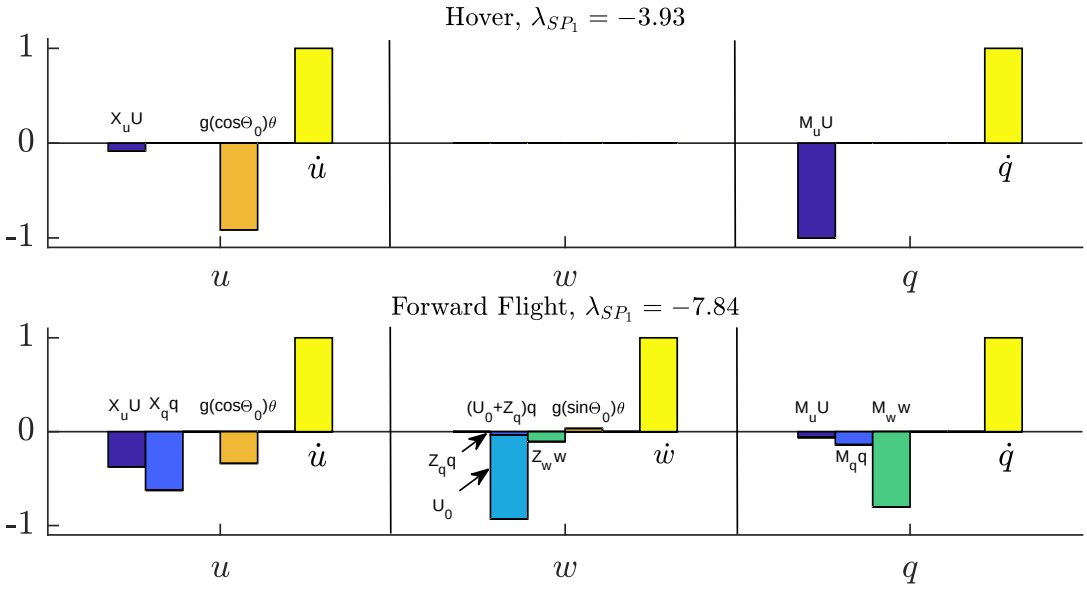

Fig. 11. Time vector comparison of the longitudinal short period eigenvalue in hover (top) and 17 kts forward flight (bottom).

essary to generate a stitched model. Table 6 shows the point model velocity spacing typically used to generate a stitched model at full scale (Ref. 2), and the resulting Froude scaled velocities (N=32.6). During the point model identification, the IRIS+ velocity oscillated around trim $\pm$ 5 kts, nearly covering the 7 kt difference in the Froude-scaled velocity spacing. Given that an IRIS+ has a nearly linear trim versus velocity gradient and the velocity variance during the identification process, two point models can accurately cover the entire flight envelope of the IRIS+. This Froude scale analysis provides excellent insight on point model spacing for stitched models of other UAVs.

Table 5. Froude Scaling of XV-15 Lateral Modal Frequencies in Hover to IRIS+ Sized Vehicle (N=34.7)

Mode	XV-15 Freq. [rad/sec]	Froude-Scaled Freq. [rad/sec]	IRIS+ Freq. [rad/sec]	Difference
$\lambda_{\text{Roll}_{1,2}}$	0.4668	2.75	2.55	7.5%
λ_{Roll_3}	0.6458	3.80	2.65	35.6%

Table 6. Typical Point Model Velocities Required for a Stitched Model of the UH-60 Compared to the Froude-Scaled Velocities (N=32.6) for a IRIS+ Sized UAV

UH-60 Velocity [kt]	Froude-Scaled Velocity [kt]
0	0
40	7
80	14
120	21
$V_{\text{max}} = 160$	$V_{\text{max}} = 28$

QUADCOPTER STITCHED SIMULATION MODEL USING STITCH

STITCH was used to generate and verify a stitched simulation model of the IRIS+ using the two flight-identified point models presented earlier. Finely-spaced trim data, which capture the variation in trim states and controls over the full airspeed range, were also included. The IRIS+ stitched model was set up for "stitching in U," which means the point model derivatives and trim data are stored and subsequently looked-up as a function of x-body airspeed U only.

Anchor Point Data

Anchor points are the specific flight conditions for which a linear model or trim data have been included in the stitched model. For the IRIS+ stitched model presented herein, the two flight-identified point models covered earlier in this paper (hover and 17 kts) were included as the anchor point models. As such, the dimensional stability and control derivatives associated with the anchor point models (see Table 3) are linearly interpolated in the stitched model between hover and 17 kts (and linearly extrapolated beyond) as a function of x-body airspeed U. Additionally, finely-spaced trim data, which capture the variation in trim states and controls for straight-and-level flight over the full airspeed range, were included as the anchor trim data. See Figure 12 for an overview of the anchor points included in the stitched model, shown here as a function of total airspeed V_{tot}.

The values of the pertinent longitudinal trim states and controls (i.e., trim z-body airspeed W_0, trim pitch attitude Θ_0, trim longitudinal stick δ_{lon_0}, and trim collective δ_{col_0}), as captured by the trim data from flight, are shown by the solid markers in Figure 13. Note that the lateral/directional trim states

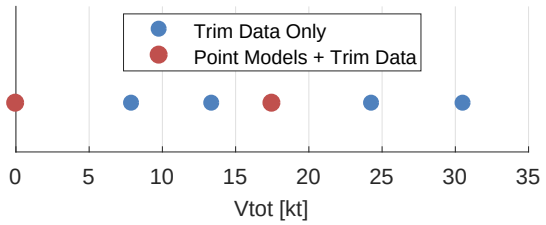

Fig. 12. Anchor points included in the stitched model.

and controls are assumed to be a constant value of zero (i.e., $V_0 = \Phi_0 = \Psi_0 = \delta_{\text{lat}_0} = \delta_{\text{ped}_0} = 0$). The raw collected trim-data trends themselves vary rather smoothly over the full airspeed range. Shape-preserving piecewise cubic interpolation was performed on the anchor trim data to produce smooth, finely-spaced data for use in the stitched model, as indicated by the dashed curves.

Trim pitch attitude Θ_0 is nearly linear over the airspeed range, as an increase in trim nose-down (i.e., negative) pitch attitude corresponds proportionally to an increase in trim airspeed. Trim z-body airspeed W_0 is analogous to trim angle of attack (i.e., $\alpha_0 = \arctan(W_0/U_0)$) and corresponds to trim pitch attitude throughout, as the trim shot data were collected in straight-and-level flight (i.e., $\alpha_0 = \Theta_0$). Trim longitudinal stick δ_{lon_0} migrates forward (δ_{lon} is defined positive aft) rather linearly from hover to approximately 13 kts, at which point it remains somewhat constant out to higher airspeeds. Trim collective δ_{col_0}, however, appears to have the opposite trend, in that it is rather flat over the low-airspeed range, then increases nearly linearly for higher airspeeds. This change in control strategy coincides with a trim pitch attitude of approximately $\Theta_0 = -15$ deg.

Stitched Model Verification

Verification of the stitched model is performed in STITCH by linearizing the stitched model at the flight conditions of the anchor point models; in this case, hover and 17 kts. This is an important step because it verifies the accuracy of the implicit speed derivatives (see Model Stitching Basic Concepts section) and their effect on the dynamic response of the stitched model. Because "stitching in U" was employed, the u-speed derivatives X_u, Z_u, and M_u are represented implicitly and must be verified against the identified results (Table 3).

Table 7 provides a comparison of the values between the implicit derivatives of the linearized stitched model and the explicit (i.e., identified) derivatives of the anchor point models at hover and 17 kts (see Table 3). There is excellent agreement in the values of X_u between the linearized stitched and the anchor point models at both hover and 17 kts. There are slight resultant values of Z_u seen in the stitched model at hover and 17 kts compared to a constant value of 0 for the anchor point models. The largest discrepancy is seen between the implicit value of M_u at 17 kts and the explicit value from the anchor point model.

Figures 14–17 show the primary on-axis pitch, roll, yaw, and heave frequency response comparisons between the linearized

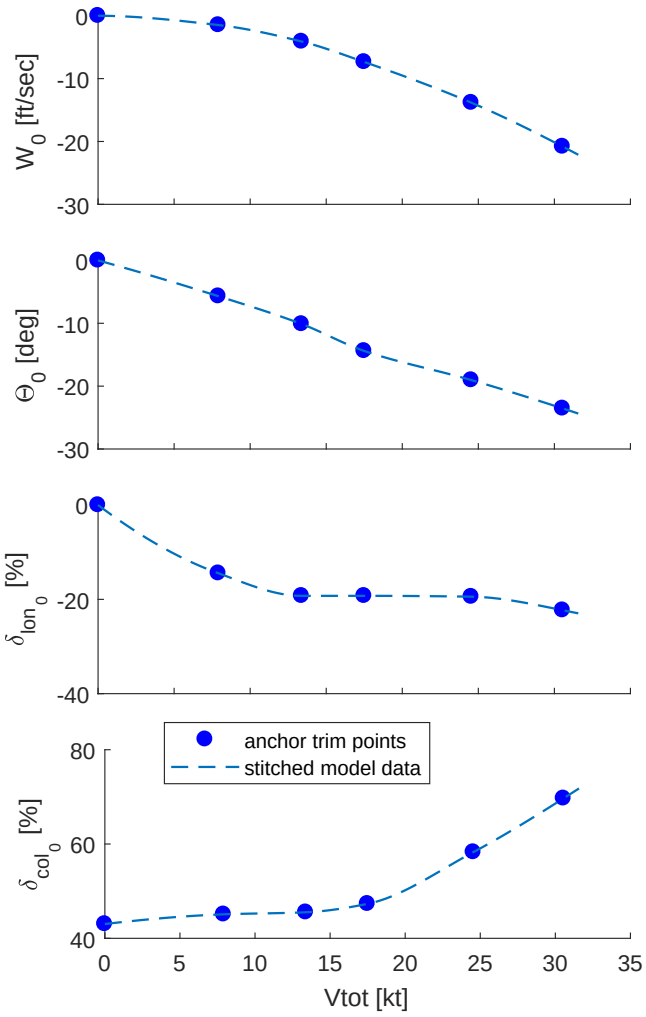

Fig. 13. Variation in trim states and controls over the full airspeed range.

stitched model and the anchor point model at hover. As can be seen in Figure 14, there is near-perfect agreement in the pitch rate response to longitudinal stick comparison between the stitched model and the hover anchor point model. The very slight disparity at low frequency is due to the small differences between the implicit and explicit values of the speed derivatives at hover, as presented in Table 7.

Figure 15 shows the roll rate response to lateral stick comparison between the stitched model and the hover anchor point

Table 7. Speed Derivatives Comparison, Implicit vs. Explicit, Hover and 17 kts

Flt Cond	Derivative	Stitched Model	Point Model
Hover	X_u	−0.3261	−0.3246
	Z_u	0.0001	0
	M_u	1.6410	1.7355
17 kts	X_u	−0.2912	−0.2956
	Z_u	−0.0451	0
	M_u	0.5183	0.3172

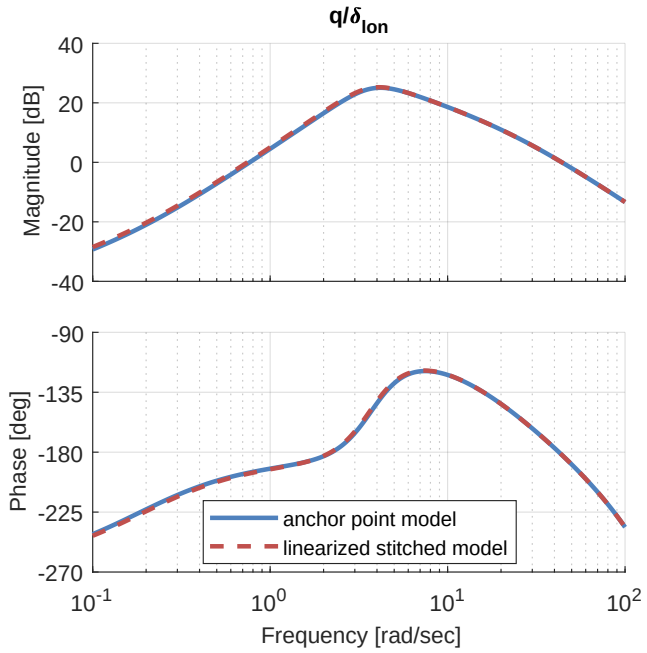

Fig. 14. Pitch rate response to longitudinal stick comparison, hover.

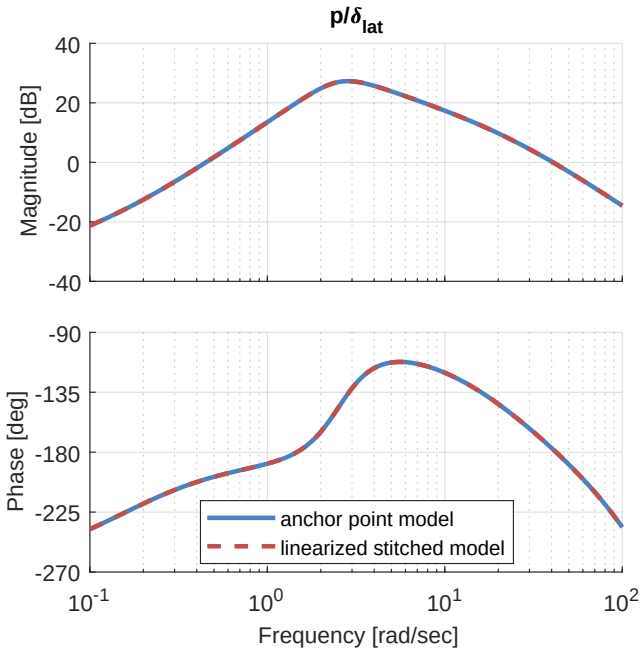

Fig. 15. Roll rate response to lateral stick comparison, hover.

model. There is perfect agreement, as expected, because the values of all lateral/directional derivatives (e.g., Y_v, L_v, L_p, etc.) in the stitched model are identical to those of the anchor point models ("stitching in U" affects only the u-speed derivatives X_u, Z_u, and M_u and the corresponding responses). Similarly, perfect agreement between the stitched model and the hover anchor point model is verified for the yaw rate response to pedal comparison shown in Figure 16 and the vertical airspeed response to collective comparison shown in Figure 17.

Figures 18–21 show the primary on-axis frequency response comparisons between the linearized stitched model and the anchor point model at 17 kts. There is overall good agreement in the pitch rate response to longitudinal stick comparison between the stitched model and the hover anchor point model, as shown in Figure 18. The disparity at low frequency is due to the differences in the values of the speed derivatives, as presented in Table 7. The speed derivatives also affect the heave response, shown in Figure 21, as the collective is the dominant control for airspeed around 17 kts. Perfect agreement between the stitched model and the 17-kt anchor point model is verified for the roll rate response and the yaw rate response, as shown in Figures 19 and 20, respectively.

In order to stabilize the unstable pitch mode at 6 rad/sec (see Table 4) the quadcopter flight control system must have a crossover frequency $\omega_c \geq 3 \times \omega_{\text{unstable}}$, based on a rule of thumb (Ref. 12), placing the crossover frequency $\omega_c \geq 18$ rad/sec for the IRIS+. Perfect agreement is realized between the stitched model and the anchor point model around crossover frequency, making any discrepancies at lower frequency insignificant.

Comparisons of the modes between the linearized stitched model and the anchor point models are presented in Table 8 and Table 9 for hover and 17 kts, respectively. The modes of the point models are those shown previously in Table 4. Agreement between the modes of the linearized stitched model and those of the anchor point models is excellent.

Table 8. Modes Comparison, Hover

Mode	Stitched Model	Point Model
Roll	$[-0.48, 2.55]$	$[-0.48, 2.55]$
Roll	(2.65)	(2.65)
Phugoid	$[-0.48, 3.70]$	$[-0.48, 3.77]$
Short Period	(3.86)	(3.93)

$[\zeta, \omega] = s^2 + 2\zeta\omega s + \omega^2$, $(a) = (s + a)$

Table 9. Modes Comparison, 17 kts

Mode	Stitched Model	Point Model
Phugoid	(-0.276)	(-0.163)
Spiral	(0.239)	(0.235)
Phugoid	(0.535)	(0.554)
Roll Aperiodic	(1.22)	(1.22)
Yaw	(1.78)	(1.78)
Short Period	(-6.05)	(-6.02)
Short Period	(8.00)	(7.84)

$(a) = (s + a)$

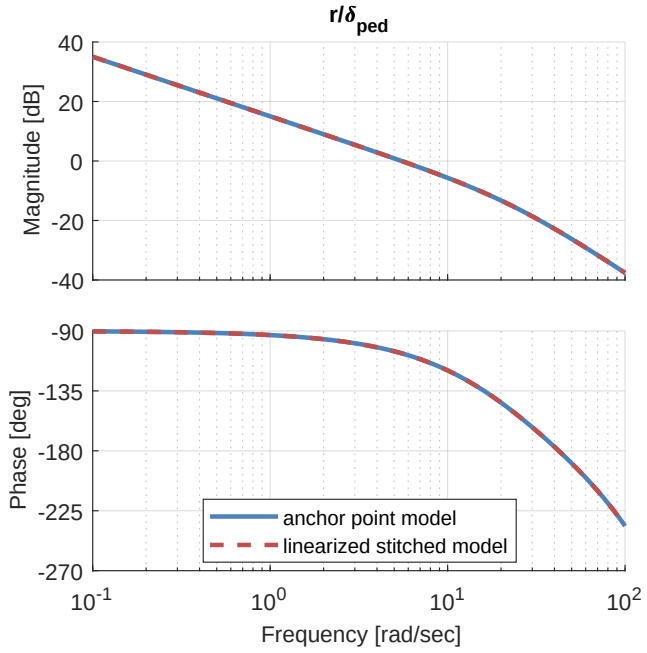

Fig. 16. Yaw rate response to pedal comparison, hover.

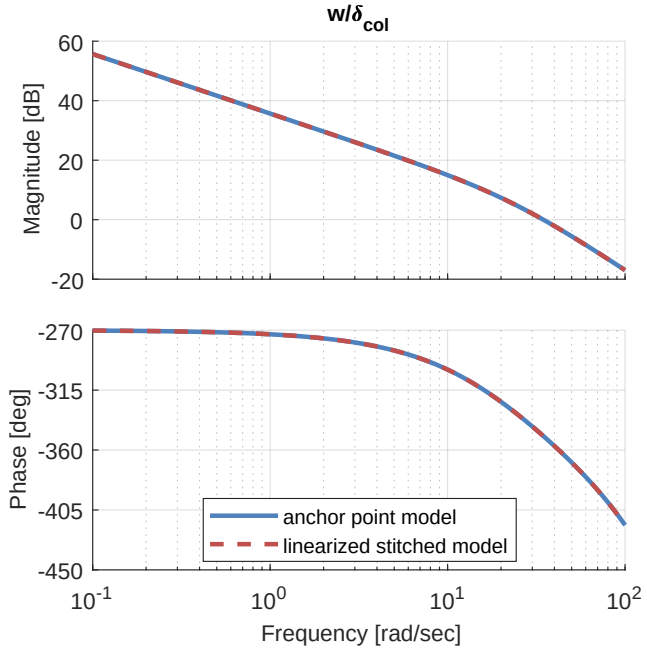

Fig. 17. z-body airspeed response to collective comparison, hover.

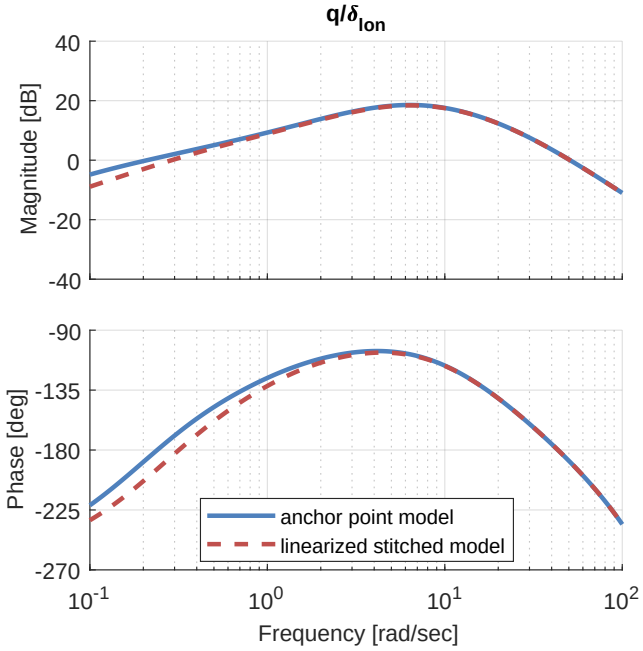

Fig. 18. Pitch rate response to longitudinal stick comparison, 17 kts.

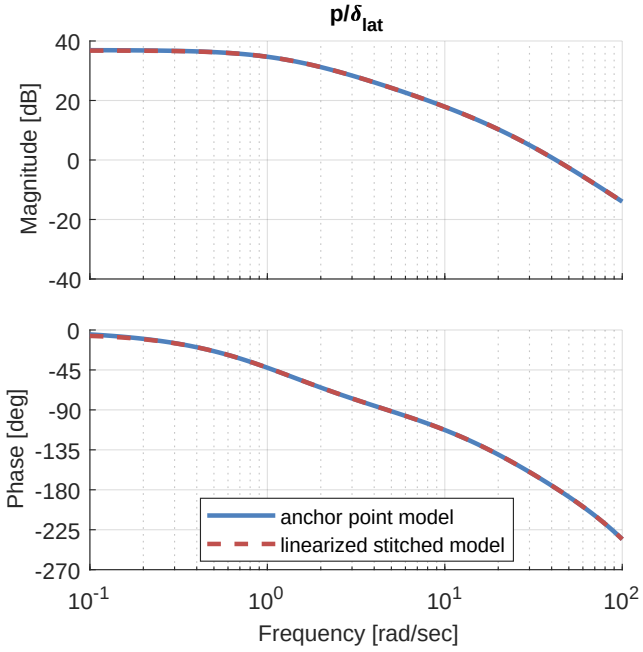

Fig. 19. Roll rate response to lateral stick comparison, 17 kts.

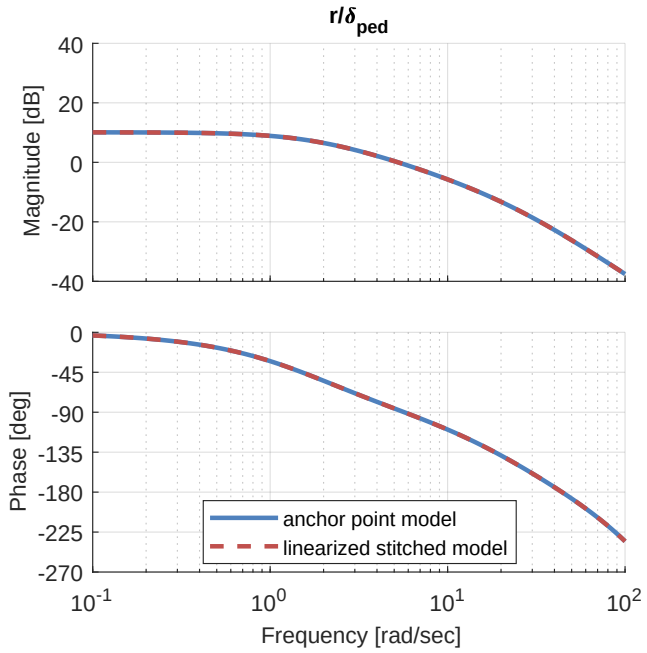

Fig. 20. Yaw rate response to pedal comparison, 17 kts.

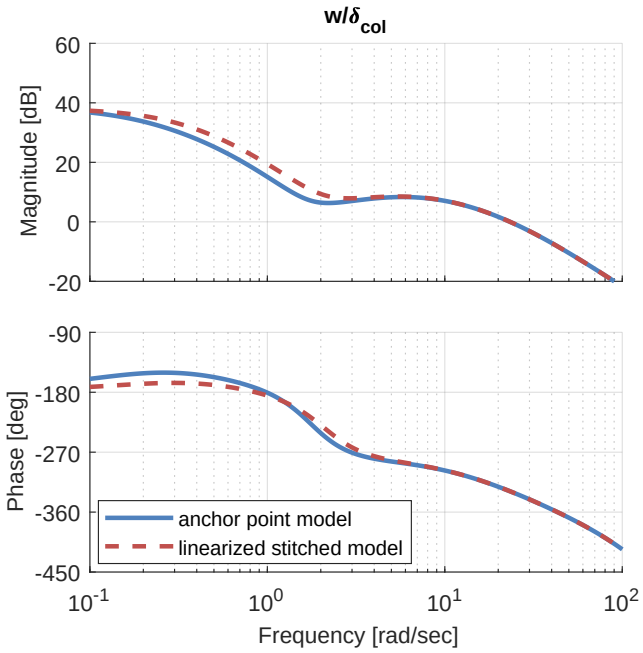

Fig. 21. z-body airspeed response to collective comparison, 17 kts.

Interpolation for Airspeed

The dynamic response of the stitched model at a mid-airspeed point of 10 kts, which is between the two anchor points of hover and 17 kts, was investigated and verified. As truth data, frequency sweeps were performed on the IRIS+ in flight at 10 kts to generate truth frequency responses. The stitched model, configured only with the two anchor point models at hover and 17 kts, was retrimmed and relinearized for the 10-kt flight condition in simulation; this requires the interpolation of the stability and control derivatives.

Figure 22 shows the pitch rate response to longitudinal stick comparison of the stitched model for the interpolated airspeed of 10 kts (shown by the red dashed response) against the truth 10-kt pitch rate response from flight (blue solid response). To provide context, the pitch rate responses of the anchor point models at hover and 17 kts are included in the figure for reference.

Two key conclusions can be gleaned from these comparisons: 1) the quadcopter's hover, 10-kt, and 17-kt dynamic responses are appreciably different; and 2) the stitched model, configured only with the anchor point models at hover and 17 kts, when linearized at 10 kts produces a frequency response that matches very well with the truth 10-kt response from flight. This confirms that the IRIS+ bare-airframe dynamics are well characterized by two point models (hover and 17 kts), and that the stitched model predicts very accurately by interpolation the bare-airframe dynamics at a mid-airspeed condition. The stitched model interpolates the dynamics continuously when simulated in real time, thus accurate dynamics are realized over the full airspeed envelope.

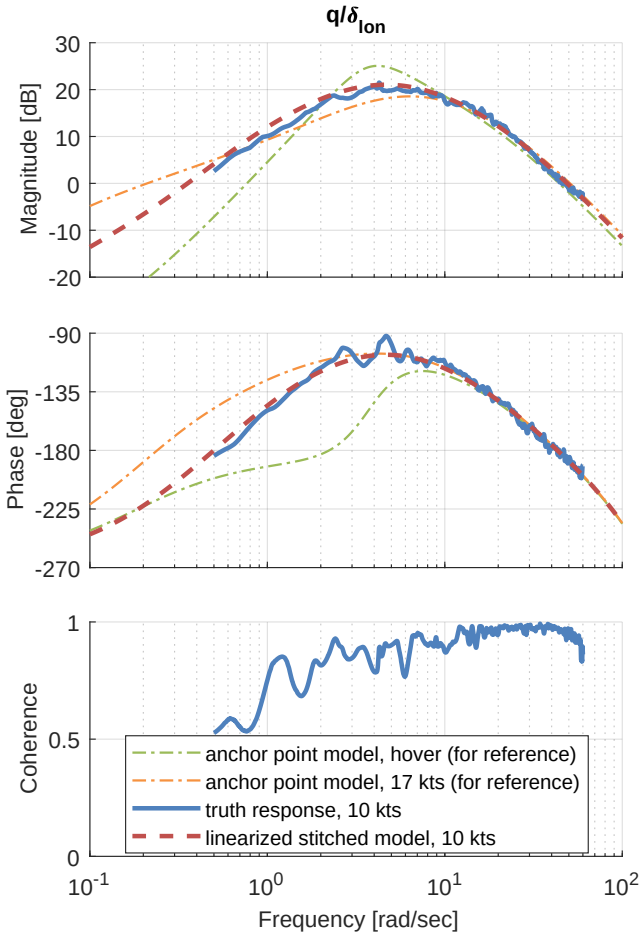

Fig. 22. Pitch rate response to longitudinal stick comparison for interpolated airspeed of 10 kts, with hover and 17-kt reference responses.

Extrapolation for Loading Configuration

The effects on trim and dynamic response of the quadcopter carrying an external payload were investigated. A heavy loading configuration was arranged by attaching a 200-gram (0.441-lb) cylindrical mass to the underside of the IRIS+ fuselage (see Figure 6), which increased the total weight from 3.168 to 3.609 lbs (a 14% increase). The mass was attached approximately 2 inches below, 1 inch left, and 0.5 inches forward of the vehicle's CG, as this was the most feasible attachment point. The placement of the payload shifted the overall CG approximately 0.275 inches down (z-axis, positive down) and slightly forward/left, based on a simple calculation of mass center (Ref. 13). Inertia values for a nominally-configured IRIS+ were obtained from Ref. 14 and used as simulation values for the nominal configuration presented herein. Inertia values for the heavy loading configuration were calculated using the parallel axis theorem. The added 200-gram mass resulted in increased roll inertia I_{xx} and pitch inertia I_{yy} by approximately 3% and 6%, respectively. The values of weight, CG offset, and inertias for the nominal and heavy loading configuration are summarized in Table 10.

Table 10. Nominal and Heavy Loading Configurations

Parameter	Nominal	Heavy
Weight [lb]	3.168	3.609
x-axis CG offset [in]	0	0.076
y-axis CG offset [in]	0	−0.122
z-axis CG offset [in]	0	0.275
I_{xx} [slug-ft^2]	0.0162	0.0167
I_{yy} [slug-ft^2]	0.00804	0.00849
I_{zz} [slug-ft^2]	0.0226	0.0227

Flight-test data of the heavy configuration were collected for use as truth data only. A trim shot covering the full airspeed range was performed on the heavy quadcopter to collect truth values of the trim states and controls as a function of airspeed. Additionally, pitch frequency sweeps were performed on the heavy quadcopter at 10 kts to generate a truth frequency response.

To verify the stitched model's ability to simulate for the off-nominal loading configuration, the simulation values of weight and CG offset were set to those of the heavy loading configuration. The stitched model, containing only the nominal anchor point data, was then retrimmed in simulation for the heavy loading over the full airspeed range from hover through approximately 32 kts.

The nominal and heavy trim-shot comparison results are shown in Figure 23. The anchor trim points (shown by the blue solid markers) and the corresponding stitched model results for the nominal loading (blue dashed curves) are repeated from those shown previously in Figure 13 for reference. The trim results of the stitched model as retrimmed (i.e., extrapolated to) the heavy loading are shown by the magenta dashed curves. Lastly, the truth trim points for the heavy loading configuration, as obtained from flight, are shown by the red triangle markers. There is excellent agreement between the extrapolated stitched model results and the truth heavy trim shot data. The increased (i.e., less-negative) trim angle of attack (analogous to W_0) and trim pitch attitude Θ_0 in forward flight for the heavy loading are well predicted by the stitched model. Trim longitudinal stick δ_{lon_0} is also well predicted. The increased trim collective δ_{col_0} necessary for hover and level forward flight of the heavy configuration is well extrapolated by the stitched model.

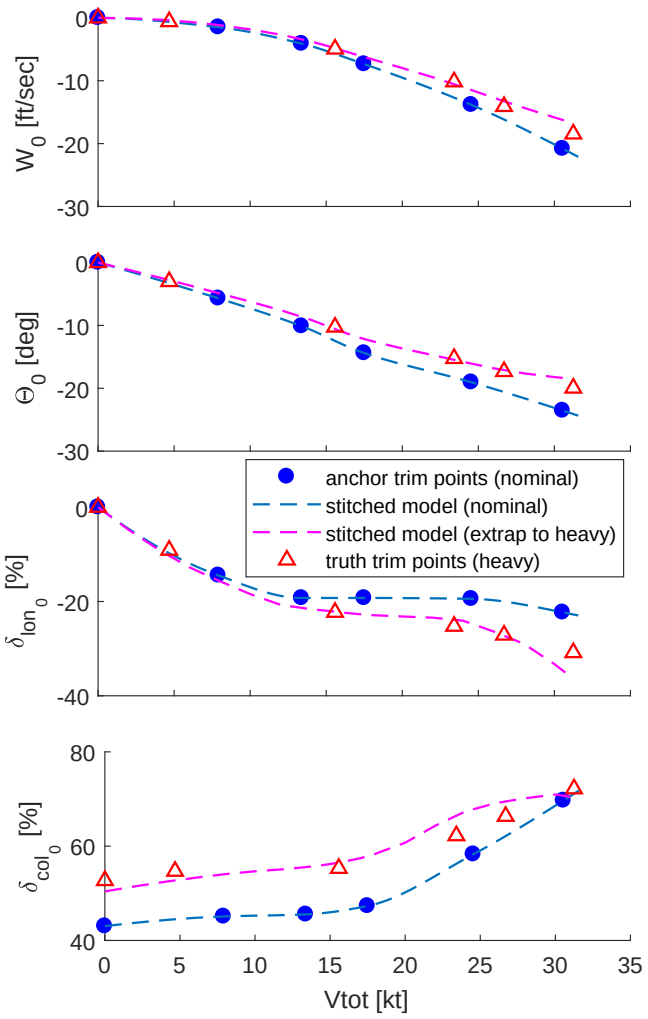

Fig. 23. Extrapolated stitched model heavy trim compared against truth heavy data from flight.

The dynamic response of the stitched model configured for the heavy loading is verified against the truth response of the heavy loading configuration from flight. Figure 24 presents the pitch rate response to longitudinal stick comparison at 10 kts of the linearized stitched model (nominal loading, for reference), the linearized stitched model as configured for (i.e., extrapolated to) the heavy loading, and the truth heavy response from flight. There is overall very good agreement between the stitched model and flight for the heavy loading configuration. The effect of the differences in trim between the nominal and heavy loading configurations (see Figure 23)

manifests as a difference in the magnitude response at low frequency (<1 rad/sec), which is clearly visible in the stitched model responses. The extrapolated heavy loading response of the stitched model compares very well with flight at low frequency, which further verifies the differences in trim between the nominal and heavy loading configurations. The magnitude response of the heavy loading in the stitched model is also slightly higher in the mid- to high-frequency range (> 1.2 rad/sec) compared to the nominal response due to the CG shift and increased mass, and matches well with the truth heavy response form flight. Generally, the pitch dynamics are very similar between the nominal and heavy configuration, and the significant difference is seen in the steady state (i.e., values of the trim states and controls).

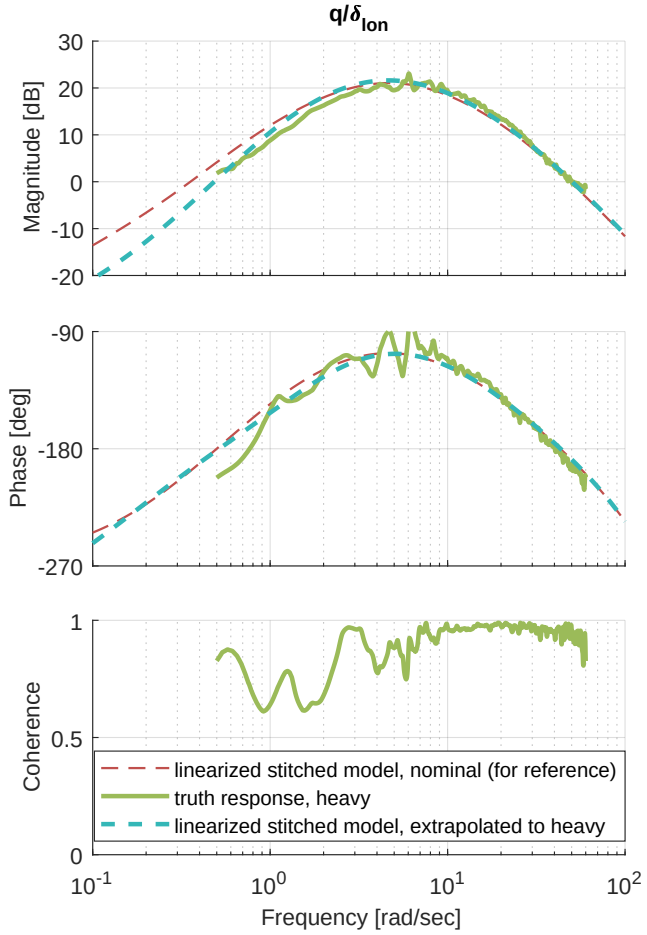

Fig. 24. Pitch rate response to longitudinal stick comparison, 10 kts, extrapolated heavy loading configuration.

Overall, the trim and dynamic response results verify the stitched model's accuracy for simulating off-nominal loading configurations with anchor point models and anchor trim data from a nominal loading configuration only. These results have positive flight-test implications for the development of UAV stitched models in that the flight testing may be conducted with a nominally-loaded UAV only.

Flight-Test Implications for Development of Small-Scale Multi-Rotor Stitched Models

This section presents flight-test recommendations for future development of stitched models involving small-scale multi-rotor vehicles, based on the IRIS+ results covered herein.

Trim Data Finely-spaced level trim data covering the entire airspeed envelope should be collected for use as anchor trim data in the stitched model. These "trim shot" data must include the trim values of the states and controls as a function of x-body airspeed U for "stitching in U".

Due to the smooth trends in trim data over the airspeed range for the IRIS+, six trim points, spaced roughly every 6 kts, adequately covered the full airspeed range form hover through approximately 32 kts. A spacing of approximately 5–7 kts is therefore recommended for the collection of trim shot data. Froude scaling may be used to determine the airspeed spacing for other vehicles.

Point Models Frequency sweeps should be performed at hover and at forward flight for the identification of state-space anchor point models. Airspeed will naturally tend to vary about the trim condition during the frequency sweep; a variation of approximately ±5 kts was observed during the frequency sweep data collection on the IRIS+. Furthermore, the identified linear point models will be accurate over some minimum range of airspeed (approximately ±10-kt accuracy was realized for the IRIS+ point models, as presented herein). Therefore, it is recommended that the identification of anchor point models be performed at a spacing of 15–20 kts for small-scale multi-rotor vehicles.

Two flight-identified point models were found herein to adequately and accurately capture the bare-airframe dynamics of the IRIS+ over its full airspeed envelope: one point model at hover, which is valid up to approximately 10 kts, and one point model at 17 kts, which is valid over approximately 10–30 kts (30 kts is the approximate maximum airspeed of the IRIS+). However, the spacing of the anchor point models does depend on the size of the vehicle and the complexity of the rotor configuration.

CONCLUSIONS

A full-envelope stitched simulation model of a quadcopter was developed using two flight-identified models of the IRIS+ and the newly-developed model stitching simulation software STITCH. The following conclusions were determined:

1. Forward-flight dynamics are significantly different than the dynamics in hover for the IRIS+. Hover dynamics are primarily comprised of translational velocity derivatives, whereas the forward-flight dynamics include both translational velocity derivatives and angular rate damping derivatives. As seen in the time vector analysis of the longitudinal short period mode, the gravity terms in

hover become less dominant in forward-flight, and the aerodynamic derivatives of the $\dot{w}$ equation have little contribution compared to the Coriolis term.

2. Froude scaling provides excellent insight into the number of point models necessary to cover the entire flight envelope of a UAV. Comparisons of the lateral modal frequencies of the IRIS+ and the full scale XV-15 have shown that Froude scaling can provide accurate predictions and insight into the UAV dynamics.

3. A stitched model configured with two flight-identified point models (hover and 17 kts), plus some finely-spaced trim data, is shown herein to adequately and accurately capture the bare-airframe dynamics of the IRIS+ over its nominal flight envelope.

4. The stitched model predicts very well by interpolation the dynamics at a mid-airspeed condition of 10 kts, as verified by a truth response from flight.

5. Trim and dynamic response results verify the stitched model's accuracy for simulating an off-nominal heavy loading configuration with anchor point models and anchor trim data from a nominal loading configuration only. Therefore, flight testing may be conducted with a nominally-loaded UAV only.

ACKNOWLEDGMENTS

The authors would like to thank Marcos Berrios for the insightful discussions and his valuable contributions to this work. Additional thanks to Anthony Gong for his help with CG calculation on the IRIS+ and for providing his flight code and data processing scripts.

REFERENCES

[1]Tischler, M. B., *Aircraft and Rotorcraft System Identification: Engineering Methods with Flight Test Examples*, American Institute of Aeronautics and Astronautics, Inc., Reston, VA, second edition, 2012.

[2]Tobias, E. L. and Tischler, M. B., "A Model Stitching Architecture for Continuous Full Flight-Envelope Simulation of Fixed-Wing Aircraft and Rotorcraft from Discrete-Point Linear Models," U.S. Army AMRDEC Special Report RDMR-AF-16-01, April 2016.

[3]Zivan, L. and Tischler, M. B., "Development of a Full Flight Envelope Helicopter Simulation Using System Identification," *Journal of the American Helicopter Society*, Vol. 55, (022003), 2010, pp. 1–15.

[4]Greiser, S. and Seher-Weiss, S., "A contribution to the development of a full flight envelope quasi-nonlinear helicopter simulation," *CEAS Aeronautical Journal*, Vol. 5, (1), March 2014, pp. 53–66.

[5]Berger, T., Tischler, M. B., Hagerott, S. G., Cotting, M. C., Gray, W. R., Gresham, J. L., George, J. E., Krogh, K. J., D'Argenio, A., and Howland, J. D., "Development and Validation of a Flight-Identified Full-Envelope Business Jet Simulation Model Using a Stitching Architecture," AIAA Modeling and Simulation Technologies Conference, AIAA SciTech Forum, Grapevine, TX, January 2017.

[6]Knapp, M. E., Berger, T., Tischler, M. B., Cotting, M. C., and Marcus, A., "Development of a Full Envelope Flight Identified F-16 Simulation Model," AIAA Atmospheric Flight Mechanics Conference, AIAA SciTech Forum, Kissimmee, FL, January 2018.

[7]McRuer, D., Ashkenas, I., and Graham, D., *Aircraft Dynamics and Automatic Control*, Princeton University Press, Princeton, NJ, 1973.

[8]Cheung, K. K., Wagster, J. A., Tischler, M. B., Ivler, C. M., Berrios, M. G., Berger, T., Juhasz, O., Tobias, E. L., Goerzen, C. L., Barone, P. S., Sanders, F. C., and Lopez, M. J., "An Overview of the U.S. Army Aviation Development Directorate Quadrotor Guidance, Navigation, and Control Project," American Helicopter Society 73rd Annual Forum, Fort Worth, TX, May 2017.

[9]*IRIS+ Operation Manual vF*, 3D Robotics, Inc., Berkeley, CA, December 2014.

[10]Berrios, M. G., Berger, T., Tischler, M. B., Juhasz, O., and Sanders, F. C., "Hover Flight Control Design for UAS Using Performance-based Disturbance Rejection Requirements," American Helicopter Society 73rd Annual Forum, Fort Worth, TX, May 2017.

[11]Mettler, B., *Identification Modeling and Characteristics of Miniature Rotorcraft*, Kluwer Academic Publishers, Norwell, MA, 2003.

[12]Tischler, M. B., Berger, T., Ivler, C. M., Mansur, M. H., Cheung, K. K., and Soong, J. Y., *Practical Methods for Aircraft and Rotorcraft Flight Control Design: An Optimization-Based Approach*, American Institute of Aeronautics and Astronautics, Inc., Reston, VA, 2017.

[13]Kane, T. R. and Levinson, D. A., *Dynamics: Theory and Applications*, McGraw-Hill, Inc., first edition, 1985.

[14]Fum, W. Z., *Implementation of Simulink Controller Design on IRIS+ Quadrotor*, Master's thesis, Naval Postgraduate School, Monterey, CA, September 2015.